

# A narrow-band, variable energy ion source derived from a wire plasma source

R Gueroult<sup>1,2</sup>, P Q Elias<sup>1</sup>, D Packan<sup>1</sup> and J M Rax<sup>2</sup>

<sup>1</sup> ONERA Palaiseau, 91761 Palaiseau, France

<sup>2</sup> LPP, Ecole Polytechnique, 91128 Palaiseau Cedex, France

E-mail: [renaud.gueroult@polytechnique.edu](mailto:renaud.gueroult@polytechnique.edu)

Received 2 March 2011, in final form 6 April 2011

Published 31 May 2011

Online at [stacks.iop.org/PSST/20/045006](http://stacks.iop.org/PSST/20/045006)

## Abstract

A low pressure wire-induced plasma source (WIPS) operated in its high-pressure mode ( $\sim 10^{-2}$  mbar) exhibits a narrow ion energy distribution function peaked at an energy corresponding to the discharge voltage. In order to take advantage of this peculiar feature, we design an electrode geometry enabling the acceleration of ions extracted from a WIPS. Probing of the obtained ion plume by means of a retarding potential analyser (RPA) demonstrates the capability of such an ion source to generate narrow-band (full width at half maximum of about 20 eV), variable energy (1 to 5 keV) ion beams. Comparison with particle-in-cell simulations of the WIPS shows that the energy spread of these ion beams is actually about 10 eV, the slight broadening being mainly the effect of the limited planar RPA energy resolution. The ion beam spot size measured at 6 cm of the ion source exit is about 3 mm for a 10  $\mu$ A He<sup>+</sup> beam at 2 keV, with a divergence of about one degree. Operating the WIPS in argon and xenon leads to similar properties for Ar<sup>+</sup> and Xe<sup>+</sup> beams, and in principle other species could also be used.

(Some figures in this article are in colour only in the electronic version)

## 1. Introduction

Shortly after the discovery by McClure [1] of the wire-induced plasma source (WIPS), Fitch [2] pointed out its relevance for the production of ion beams. Indeed, the simple wire-cylinder electrode configuration of the WIPS allows the operation of a low-pressure gaseous discharge at low applied potential by means of an efficient electron confinement, limiting in turn the gas flow requirement. Moreover, the electron confinement being strictly electrostatic, the WIPS does not require any magnetic coils as opposed to low pressure discharge devices relying on magnetic confinement such as the Penning discharge.

The first WIPS-based ion guns [2–4] made use of a two-wire WIPS configuration proposed earlier by McIlraith [5]. This configuration gives rise to a pendulum motion of electrons perpendicularly to the axis of the wire anodes, which extends the electron mean free path and thus permits the further decrease of the working gas pressure. Current densities of a few 100  $\mu$ A cm<sup>-2</sup> were measured at 10<sup>-4</sup> mbar in argon. Despite its benefits, this kind of ion gun still has major drawbacks. To begin with, the energy of this beam has to be controlled by the anode potential. Considering that

only a small fraction of ions exits the source, increasing the anode potential rapidly increases the power requirement, even if only a limited part of it is given to the beam. Furthermore, the obtained ion beam has a broad-band energy spectrum [3], which is undesirable for some applications (diagnosis, calibration, etc).

The possibility of extracting ions from a wire source has given rise to the concept of a secondary emission electron gun (SEEG) [6–8]. A negatively biased electrode is placed in a second chamber, connected to the main chamber via a small diaphragm. Ions exit the main chamber through the diaphragm, then accelerate towards the electrode, and eventually generate electrons by secondary emission processes. Electrons are accelerated in the opposite direction, cross the diaphragm and the main chamber and finally exit it through a second diaphragm. The negatively biased electrode permits modulation of the electron beam energy almost independently of the beam current. Nevertheless, the efficiency of these electron guns, in term of beam current, has been shown [9] to depend strongly on the WIPS operating conditions. In the SEEG, the beam current is partly tied to the ion current impacting the emitting electrode. Thus increasing the efficiency of the SEEG requires a good characterization

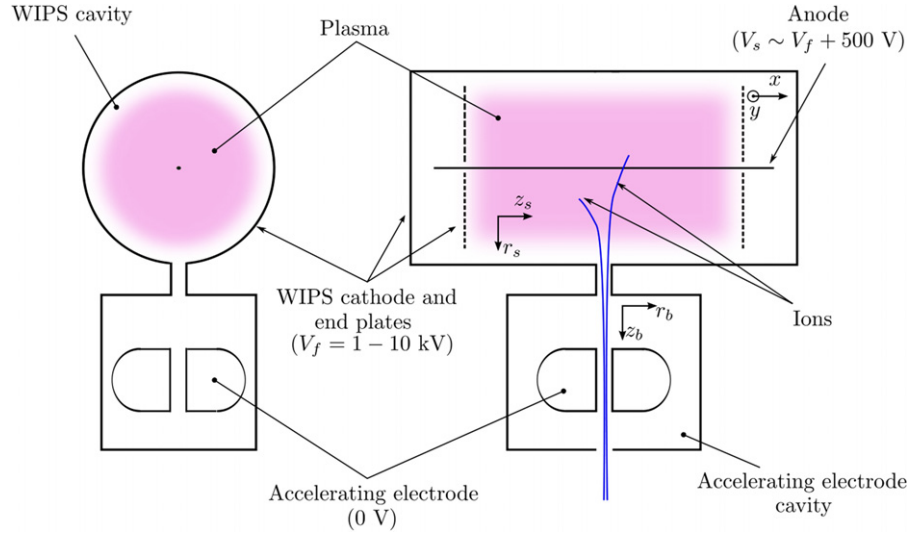


**Figure 1.** Ion source concept. Ions are extracted from a wire plasma source and accelerated towards a grounded electrode before escaping through a hole.

the ion beam extracted from the WIPS, in terms of energy and spatial extension. Incidentally, this characterization would provide a direct evaluation of the WIPS as a standalone ion source. Indeed, the idea here is to add to Fitch's concept of ion extraction the modularity offered by an additional electrode controlling ion acceleration, in a way very similar to the SEEG.

In this paper, we show that an ion source derived from a wire discharge produces low divergence ( $<2^\circ$ ), narrow-band ion beams of variable energy (200 to 5 keV), and can be operated in various gases. First, the wire discharge operating conditions most favourable to the generation of a narrow band ion beam are identified using particle-in-cell (PIC) simulations in section 2. Then, the experimental setup enabling the extraction and acceleration of ions and the diagnosis equipment are presented in section 3. Finally, experimental results dealing with the energy spread and the spatial spread of the ion beam are given and discussed in section 4.

## 2. Operating principles

The ion source consists of a SEEG in which the accelerating electrode is drilled to let ions pass through it. As shown in figure 1, ions are extracted from the wire discharge chamber through a diaphragm drilled in the WIPS cathode and are accelerated towards a grounded electrode. The idea is that instead of generating electrons by means of secondary emission processes as in a SEEG, ions escape the device through the hole drilled in the accelerating electrode.

Considering that the pressure in the accelerating electrode cavity is low, collisional effects should be limited. Consequently the energy distribution function  $f_i^s$  of ions exiting the ion source should be more or less the same as that of ions going through the diaphragm connecting the two chambers, but shifted by the acceleration voltage. Assuming that the presence of the accelerating electrode does not modify significantly the electric field inside the wire discharge chamber, an estimate of  $f_i^s$  can be obtained by studying a single wire discharge without a diaphragm.

This assumption presupposes a relative decorrelation between the ion production inside the WIPS and the acceleration process.

A PIC modelling of the dc low pressure ( $10^{-4}$ – $10^{-2}$  mbar) wire discharge in the milliamper range has been reported elsewhere [10]. The two experimentally observed modes of discharge—diffuse above a threshold pressure and constricted below—have been reproduced numerically in helium, the transition between these modes occurring for a pressure of about  $5.8 \times 10^{-2}$  mbar for a 1 mA discharge current. Hints have been shown indicating that the diffuse and constricted modes of the low pressure wire discharge could potentially be, respectively, some kind of normal and obstructed regime of a strongly asymmetric discharge between coaxial electrodes. PIC simulation results yield the ion radial velocity distribution function

$$f_{v_r}^s = \int \int f(v_r, v_\theta, v_z) dv_\theta dv_z$$

in the WIPS discharge chamber frame ( $r_s, \theta_s, z_s$ ). In particular, the ion radial velocity distribution function  $f_{v_r}^s$  can be obtained on the surface  $S_e$  of the WIPS cathode corresponding to the extraction area, and that for various pressure values. As illustrated in figure 2, the shape of  $f_{v_r}^s$  is fundamentally different depending on the WIPS discharge mode. Indeed, when the discharge is diffuse (high pressure mode),  $f_{v_r}^s$  peaks at the discharge potential, decreasing to zero at a few per cent of the discharge voltage. Conversely, in the constricted mode (low pressure),  $f_{v_r}^s$  is much broader. The fact that  $f_{v_r}^s$  is much broader at low pressure might look counter-intuitive as one might think that higher pressure and thus higher collision rates should lead to broader spectrum. Nevertheless it can be explained by looking at the evolution of both the ionization  $K(r_s)$  and the electric potential  $V(r_s)$  radial profiles in the discharge longitudinal mid-plane, in both modes. Using a 1D radial assumption is justified as both the ionization  $K(r_s, z_s)$  and electric potential fields  $V(r_s, z_s)$  are almost independent of  $z_s$  in a volume corresponding to a longitudinal slice centred on the extraction surface  $S_e$ . In the diffuse mode, the potential

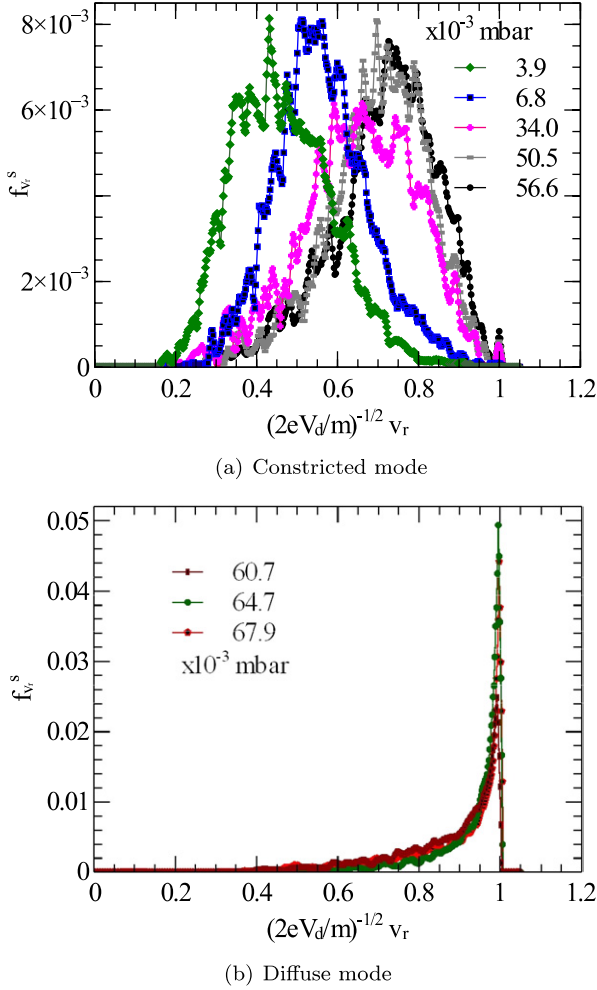


**Figure 2.** Normalized radial velocity distribution function  $f_{v_r}^s$  of ions impacting the surface of the cathode corresponding to the extraction area  $S_e$  for various pressures. Curves corresponding to the diffuse mode (b) are peaked for an energy corresponding to the WIPS discharge voltage ( $V_d$ ), whereas distribution functions for the constricted mode (a) are much broader.

remains nearly equal to the anode potential on a few tens of anode radii whereas it quickly drops in the constricted mode. In the meantime, irrespective of the discharge mode, ionization is limited to a cylinder of 10 to 20 anode radii around the anode, and whose radius slightly increases with pressure. Thus, even if the ionization region expands a little further in the high-pressure mode, many of the ions have an initial potential energy of the order of the discharge voltage in the diffuse mode. On the other hand, the ionization covers a region where the electric potential evolves quickly in the constricted mode, giving rise to a broader spectrum.

In order to quantitatively illustrate this feature, let us introduce the normalized electric potential decrease  $\delta_V$  and the ratio  $\Omega$  of the ionization rate in a cylinder of radius  $r_s$  over the total ionization rate in the discharge as

$$\delta_V(r_s) = 1 - \frac{V(r_s)}{V_a} \quad \text{and} \quad \Omega(r_s) = \frac{\int_{R_a}^{r_s} K(r') 2\pi r' dr'}{\int_{R_a}^{R_c} K(r') 2\pi r' dr'} \quad (1)$$

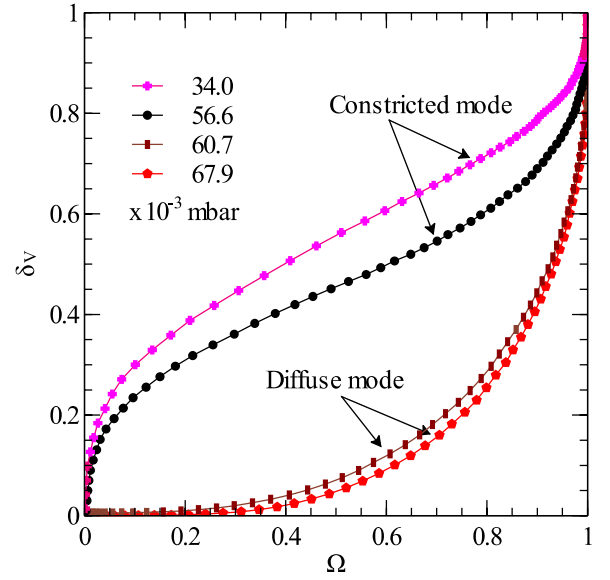


**Figure 3.** Normalized electric potential decrease  $\delta_V(r_s) = 1 - V(r_s)/V_a$  as a function of the ratio of the ionization rate in a cylinder of radius  $r_s$  over the total ionization rate in the discharge  $\Omega(r_s)$  for various pressure conditions corresponding to the two distinct modes of discharge.

where  $K(r')$  is the volumic ionization rate at radius  $r'$ ,  $V_a$  the anode potential, and  $R_a$  and  $R_c$  the WIPS anode and cathode radii. As shown in figure 3, in the diffuse mode about three ions out of four are generated in a region where the electric potential is higher than 80% of the discharge voltage. On the other hand, in the constricted mode at most 50% of the ions are generated in a region where the electric potential is greater than half of the discharge voltage. Moreover, curves corresponding to the diffuse mode (high pressure) are very close to each other, as opposed to those of the constricted mode (low pressure). This difference explains the distinct behaviour of the  $f_{v_r}^s$  curves set in each mode observed in figure 2. Indeed the dispersion of the energy corresponding to the  $f_{v_r}^s$  maximum in the constricted mode results from the vertical shift existing between the  $\Omega$  versus  $\delta_V$  curves.

The strong difference observed on  $f_{v_r}^s$  between the diffuse and the constricted modes explains why the spectrum properties of ions exiting the ion source should depend strongly on the operating conditions of the WIPS. In particular, the high-pressure mode of the WIPS seems the most adequate to produce narrow-band ion beams. Moreover, the strong dependence of the SEEG efficiency on the operating conditions partly results from the sudden variation of the ion beam properties with the WIPS mode transition. Indeed, since the coefficient of secondary emission by ion impact is an increasing function of the ion energy on the energy range considered [11], a narrow-band ion beam leads to a better efficiency than a broad-band one for a given anode voltage.

### 3. Experimental setup

#### 3.1. Ion source prototype

The wire plasma source is made of a wire anode, a cylindrical cathode and two plates at each end of the cathode providing

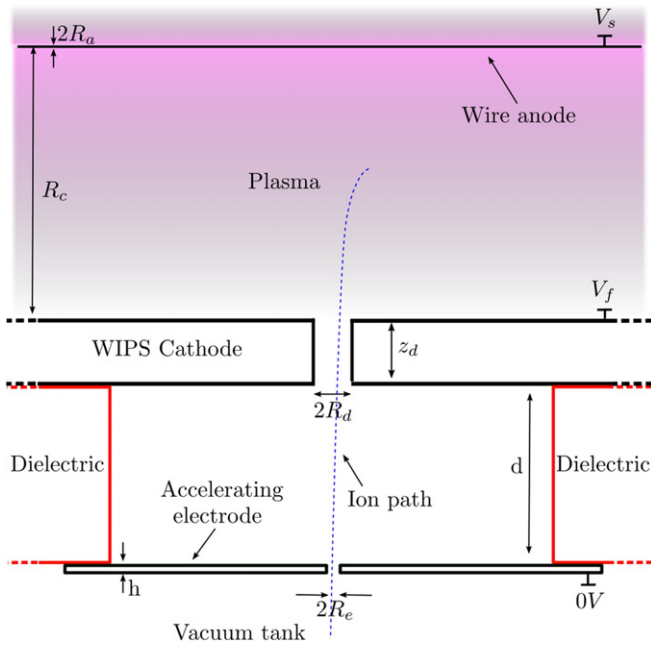


**Figure 4.** Design of the extraction and acceleration region.

longitudinal confinement of electrons. The anode is a  $R_a = 0.1$  mm radius tungsten wire stretched on the axis of the aluminium cathode. The radius and length of the cathode are  $R_c = 2.5$  cm and  $L = 10$  cm, respectively. A silica window is placed at one end of the cylinder to control visually the discharge radial extension. As shown in figure 4, a  $R_d = 4$  mm radius,  $z_d = 6$  mm long diaphragm connects the wire discharge chamber to a second chamber, in which the accelerating electrode is located. The accelerating electrode is an  $h = 1$  mm thick brass disc, having a concentric hole of radius  $R_e = 4$  mm, and placed at a distance  $d = 1.6$  cm from the diaphragm exit. Because of its relatively low secondary emission coefficient compared with aluminium [12], brass is used to limit secondary emission of electrons resulting from ion impact on the accelerating electrode.

As opposed to the SEEGs, the accelerating electrode cannot be negatively biased, or else ions would return to it. The anode and cathode of the WIPS are consequently positively biased to potentials  $V_s$  and  $V_f$ , respectively— $V_s$  being typically a few hundred volts higher than  $V_f$ —while the accelerating electrode is grounded. The WIPS end plates are connected to the cathode.

The ion source is mounted on a 2 m long, 0.8 m diameter vacuum tank, pumped by a HiPace 2300 Pfeiffer turbo-molecular pump ( $2000 \text{ L s}^{-1}$  in  $\text{N}_2$ ). The amount of gas (helium, argon, xenon) fed into the wire discharge chamber is controlled using an EL Flow Bronkhorst mass flow meter and the pressure in the WIPS chamber measured by a Baratron capacitive gauge. The mass flow meter and the pressure gauge are connected to the wire source by means of vinyl tubing. The lengths of these tubings have to be carefully designed to avoid undesirable breakdown. In our case, the setup was designed to operate with  $V_f \leq 5$  kV in helium at  $10^{-2}$  mbar in the WIPS cavity. The pressure in the vacuum tank is about a hundred times lower than that in the WIPS cavity.

### 3.2. Data acquisition bench

The complete setup is sketched in figure 5. The equipment list can be divided into two groups according to their usage.

The first one is dedicated to the recording of the ion source operating conditions. The WIPS anode and cathode potentials ( $V_s$  and  $V_f$ ) are recorded using P6015A Tektronix high voltage probes. The direct component of the wire discharge current  $I_s$  is measured using a Hall current probe while the non-existence of high frequency oscillations is assessed using a Rogowski probe. All signals are monitored on a LeCroy Wave jet 100 MHz oscilloscope.

The rest of the equipment is used to characterize the ion beam produced by the ion source. The axial velocity distribution function of the ion beam is probed using a retarding potential analyser (RPA), which consists of four polarized grids and a collector. The inter-grid distance is 7 mm. The first grid is grounded, acting mainly as an attenuator. The second grid is negatively biased to  $-25$  V to repel electrons coming from the vacuum tank. The third grid is the analysing grid. The last grid, called the suppressor grid, is used to suppress secondary emission electrons coming from the collector and the three first grids. To be efficient, it has to be polarized at a potential lower than the potential of the electrode on which secondary emission occurs minus the typical energy of secondary emission electrons. It is consequently negatively biased to  $-30$  V, which is enough to suppress electrons coming from the first and third grids and the collector, as well as a large number of electrons coming from the second grid. The RPA housing is grounded, with a 1.25 mm radius hole on its top. A National Instruments PCI 6251 data acquisition card is used to generate a ramp input signal for the power supply dedicated to the polarization of the RPA analysing grid. The sample rate varies between 10 and 500 Hz with a 2 V resolution. The input signals of the acquisition card are the analysing grid potential measured by means of a P6015A Tektronix high voltage probe and filtered using a SIM965 Stanford Research Systems analogue filter, as well as the current reaching the collector measured using a Keithley 485 pico ampere meter.

A global python script controls the displacement of an AXMO three-axis translation stage on which is placed the RPA as well as the National Instruments BNC 2110 block using the NI-DAQmx library, hence permitting a fully automated 3D scan of the ion beam.

## 4. Results and discussion

Experimental characterization of the ion beam exiting the ion source is made using the setup described in section 3. To begin with, measurements are made on the axis of the ion source to determine the energy spread of the ion beam. Then a three-dimensional RPA analysis of the ion plume is realized to characterize its spatial extension for various operating conditions. An estimate of the ion beam current is obtained using the current density maps.



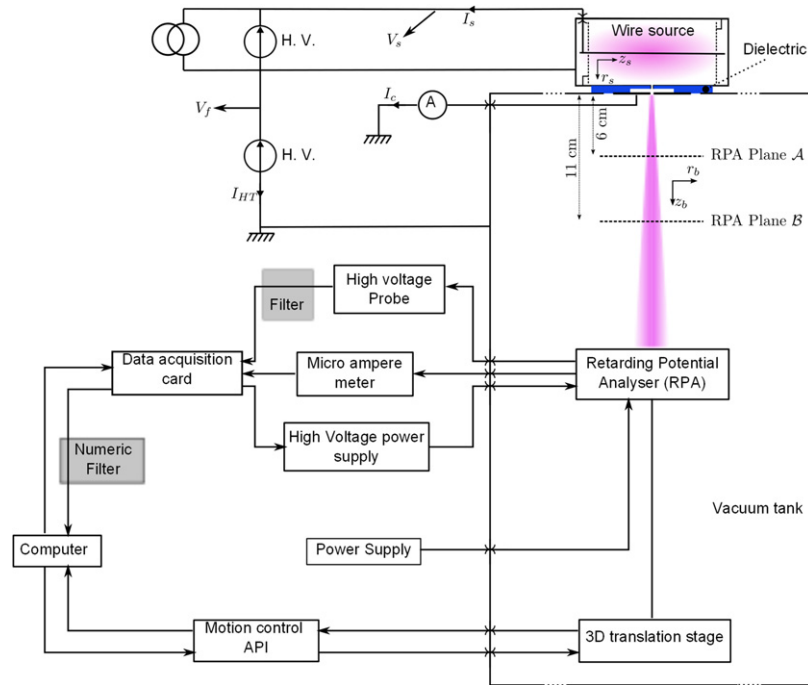


**Figure 5.** Sketch of the experimental setup.

#### 4.1. Ion beam energy spread

A single point RPA scan gives access to the local distribution function of the ion velocity projected on the RPA axis. The RPA is therefore aligned on the ion source axis in order to obtain the distribution function  $f_{v_z}^b$  of the  $z_b$  velocity component in the beam frame ( $r_b, \theta_b, z_b$ ).

Figure 6 presents the on-axis shape of  $f_{v_z}^b$  obtained at 6 cm of the accelerating electrode for each mode of discharge of the WIPS and a 2 kV accelerating voltage. The high pressure mode curve is plotted along with the PIC simulation distribution function  $f_{v_r}^s$  shifted by the acceleration voltage  $V_f = 2$  kV. Spectrum shapes match very well the predictions of the model given in section 2, justifying *a posteriori* the hypothesis of relative decorrelation existing between ion production in the WIPS and acceleration.

As the wire discharge may be operated in various gases, beams of various ionic species can be obtained. Experimental measurements show that the global WIPS behaviour remains unchanged when using neon, argon or xenon instead of helium, except for a variation of the pressure corresponding to the mode transition. Hence the energy distribution function of other ionic species beam should not be significantly different from the one of an  $\text{He}^+$  beam. The distribution function  $f_{v_z}^b$  of a  $\text{Xe}^+$  beam plotted in figure 7 confirms that the narrow band property is indeed not a specific feature of an  $\text{He}^+$  beam, as long as the discharge is operated in its diffuse mode. The slightly higher energy beam observed for  $\text{Xe}^+$  for the same accelerating voltage  $V_f$  results from a higher WIPS discharge voltage  $V_d$  in xenon.

Despite a close match between the experimental energy distribution function and the PIC predictions, a close up of figure 6 (inset) shows that the width of the experimental peak is slightly larger than the numerical one. In terms of applications

such as calibration, being able to narrow the energy spectrum is particularly interesting. It is therefore essential to discriminate between the actual beam energy spectrum spread and the broadening induced by the experimental operation of the device.

Three different origins of broadening can be identified. First, the wire discharge is current driven, and thus the WIPS discharge voltage  $V_d = V_s - V_f$  is regulated to maintain the current  $I_s$  to its set point. It induces variations of  $V_d$  by a few volts around its mean value. Those variations being at frequencies higher than the acquisition frequency, the RPA signal is equivalent to the sum of multiple contributions of beams having an energy varying like  $V_s$ . Second, the ripple of the RPA analysing grid power generator limits the acquisition resolution by acting as a moving average on the distribution function. Despite having different origins, these two phenomena have similar effects on the theoretical distribution function and these effects are independent of the ion beam energy. The third cause of broadening is related to the intrinsic resolution of a planar RPA. As described by Enloe [13], a RPA scan of an ideal mono-energetic beam of energy  $E$  would see its width broaden as

$$\frac{\Delta E_e}{E} = 1 - \frac{2\pi(d/a) - \ln 4}{2\pi(d/a) - 2 \ln[2 \sin(\pi r/a)]} \quad (2)$$

where  $r$  is the radius of an RPA grid wire,  $a$  is the distance between grid wires and  $d$  is the distance between the RPA grids. This broadening results from the inability of grid wires to generate perfectly flat equipotential surfaces. The total beam energy broadening  $\Delta E$  is hence the convolution of the power supply induced broadening  $\Delta E_n$  and the RPA resolution induced broadening  $\Delta E_e$ ,  $\Delta E_n$  itself being the convolution of the  $V_d$  regulation induced broadening  $\Delta E_n^{V_d}$

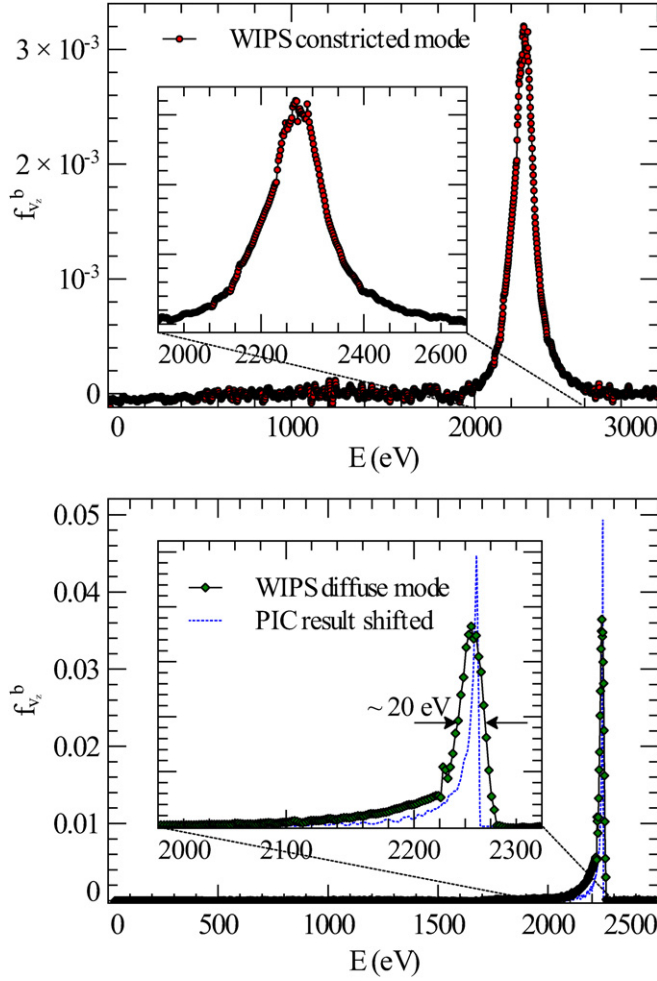


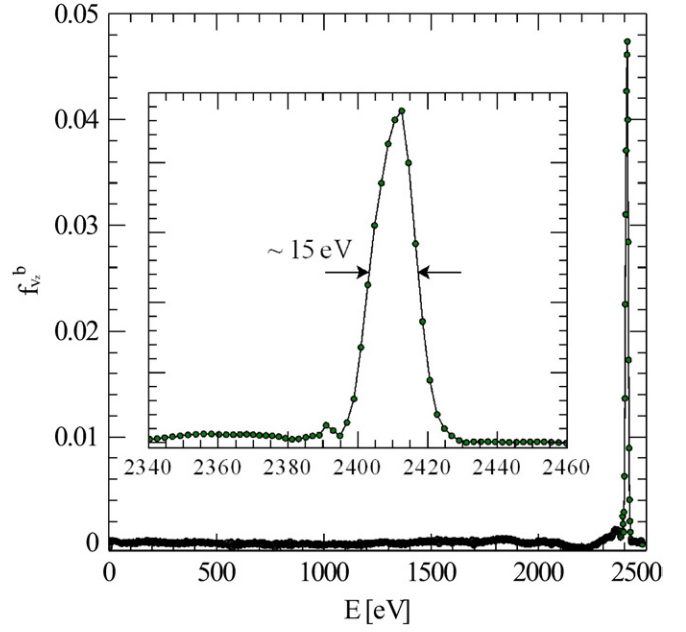
**Figure 6.** Distribution function  $f_{v_z}^b$  obtained by RPA measurement at 6 cm of the accelerating electrode for each WIPS mode of discharge and a 2 kV accelerating voltage. The narrow-band spectrum peculiar to the diffuse mode is obtained at high pressure whereas a broad-band spectrum is produced when pressure is decreased below the threshold value.

and the RPA analysing grid power supply ripple induced broadening  $\Delta E_n^{RPA}$ .

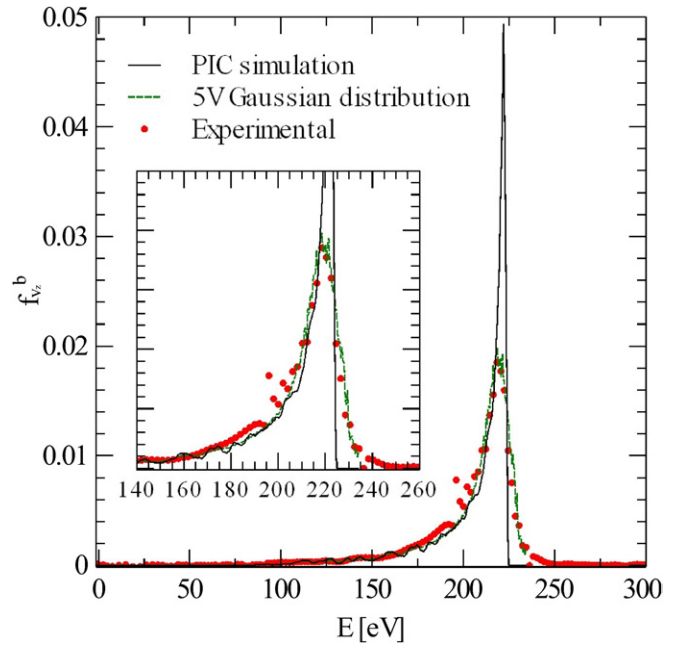
To distinguish between the two contributions  $\Delta E_n$  and  $\Delta E_e$ , the distribution function for zero acceleration is measured and compared with the PIC predictions. The experimental peak full width at half maximum (FWHM) featured in figure 8 is about 13 eV. As the beam energy is limited ( $\sim 225$  eV), the RPA resolution error  $\Delta E_e$  is reduced to about 1.4 eV. The observed broadening is very well reproduced by summing the contribution of PIC profiles with a 5 V standard deviation Gaussian distribution of energies. Considering the standard deviation of  $\Delta E_n^{V_d} \sim 3$  V observed experimentally for the  $V_d$  signal and the  $\Delta E_n^{RPA} \sim 3$  V ripple of the RPA analysing grid power generator, the standard deviation  $\sigma = 5$  V used in this plot agrees very well with the theoretical value

$$\sigma = \sqrt{(\Delta E_n^{V_d})^2 + (\Delta E_n^{RPA})^2 + (\Delta E_e)^2} \sim 4.45 \text{ V.}$$

As the beam energy increases,  $\Delta E_e$  becomes larger and larger whereas  $\Delta E_n$  remains constant. The convolution



**Figure 7.**  $\text{Xe}^+$  energy distribution function  $f_{v_z}^b$  for  $V_f = 2$  kV. The narrow-band property identified for  $\text{He}^+$  is recovered for  $\text{Xe}^+$ . The WIPS operating conditions are  $I_s = 4$  mA and  $V_d = V_s - V_f \sim 415$  V.

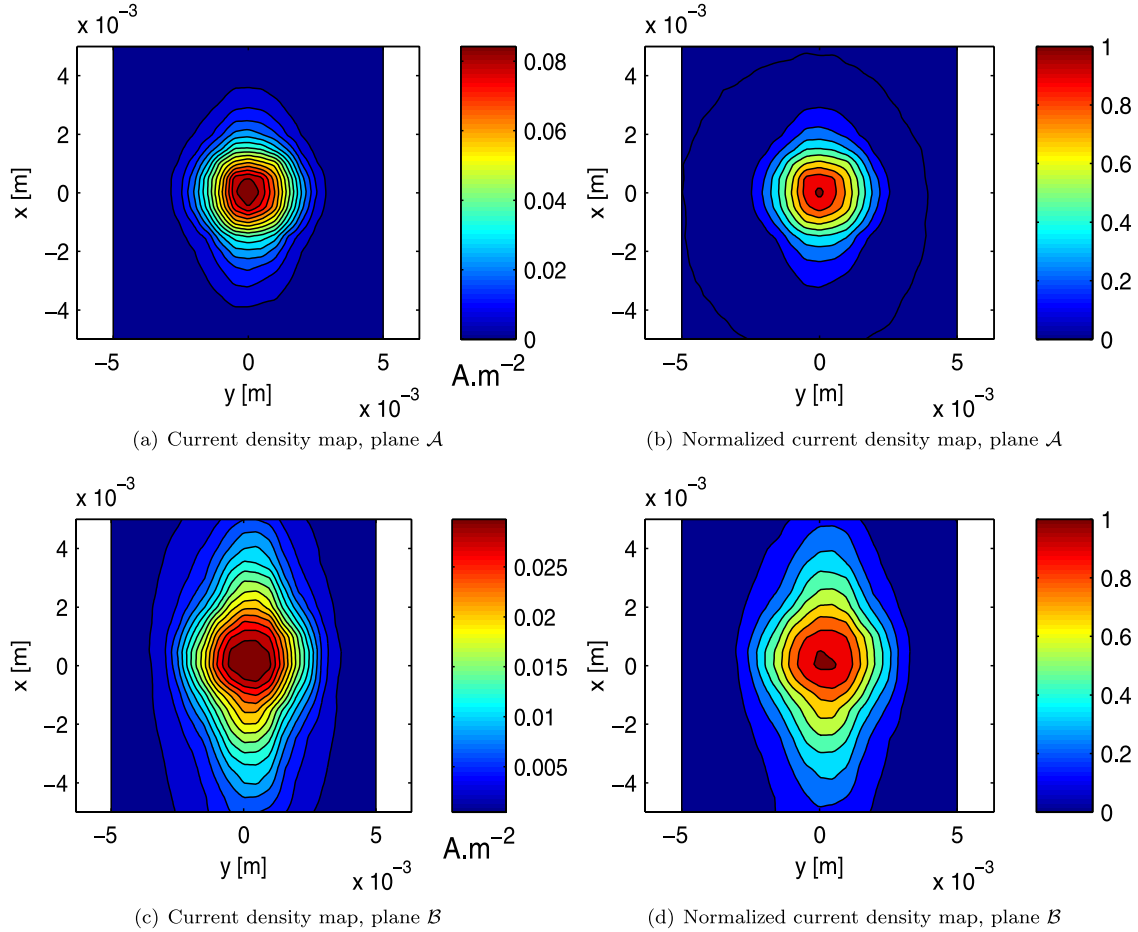


**Figure 8.** Distribution function  $f_{v_z}^b$  for  $V_f = 0$  kV along with PIC prediction as well as the sum of PIC predictions for energies spread over a Gaussian distribution ( $\sigma = 5$  V).

of  $\Delta E_n$  and  $\Delta E_e$  therefore tends to  $\Delta E_e$  as  $E$  increases. Experimental data synthesized in table 1 confirms the scaling of the beam energy spectrum width with the beam energy. The small difference between the observed energy spectrum width and the theoretical values  $\Delta E_e$  obtained using (2) is indeed relatively independent of the beam energy. Moreover, the difference of about 6 eV agrees very well with the prediction of the PIC calculations.

**Table 1.** Ion energy FWHM for various accelerating potentials. The slight increase is in good agreement with the RPA resolution decrease  $\Delta E_e$  described by Enloe [13] ( $r = 7.5 \times 10^{-5}$  m,  $a = 4.5 \times 10^{-4}$  m,  $d = 7 \times 10^{-3}$  m).

$V_s$ (V)	2225	2725	3225	3725	4225	4725	5225
FWHM (eV)	19	22	26	30	32	34	38
$\Delta E_e$ (eV)	13.7	16.8	19.9	22.9	26.0	29.1	32.2
Difference (eV)	5.3	5.2	6.1	7.0	6.0	4.9	5.8

**Figure 9.** He<sup>+</sup> beam current density ((a), (c)) and normalized current density—current density over the maximum current density—((b), (d)) maps at, respectively, 6 cm (plane A) and at 11 cm (plane B)) of the accelerating electrode (2 kV).

To summarize, ion beams having a distribution function FWHM of a few tens of electron volts have been measured. Operating the WIPS in its high-pressure mode in various gases confirms that ion beams of various ionic species featuring the same narrow band property can be obtained. Moreover, as the slight broadening compared with the PIC predictions is largely due to the acquisition loop, the effective energy distribution FWHM of an ion beam extracted from the ion source should be about 10 eV, and potentially lower using a voltage driven WIPS.

#### 4.2. Ion beam spatial spread

In order to characterize the beam spatial extension, RPA measurements are made point by point in planes parallel to the accelerating electrode at, respectively, 6 mm (plane A) and 11 mm (plane B) from it, as shown in figure 5. Typical current density and normalized current density—current density over

the maximum current density—maps (441 points by plane) obtained are given in figure 9. The increase in the beam spot size between planes A and B results from the divergence of the beam.

Using the transmission coefficient of each RPA grid, a 10  $\mu$ A estimate of the ion beam total current is deduced from the current density map plotted in figure 9, whereas an ion current  $I_c \sim 1 \mu$ A is measured on the accelerating electrode. The spatial extension of an He<sup>+</sup> beam at  $V_f = 2$  kV in plane A is such that 50% of the total beam current is contained in a 1.6 mm radius cylinder and 80% in a 2.7 mm radius cylinder. Spatial extension of the ion beam are synthesized in table 2 for various conditions. Whereas the spatial extension of the beam increases with the acceleration voltage, the divergence of the beam—computed from the 80% cone—decreases from 1.3° at 2 kV to 1.0° at 3 kV.

In addition to the current density maps, RPA scans give access to the energy distribution function of ions as a function

of the position in the beam. The distribution function isolevels along the  $x$  and  $y$  axes plotted in figure 10 indicate that the almost mono-energetic property observed along the ion source axis in section 4.1 is a global property of the ion beam. Indeed the energy distribution function remains peaked at  $V_s$  independently of the position in the beam. The slight decrease in the beam energy, resulting in a small curvature of the isocontours in figure 10, as the measurement point moves away from ion source axis is a consequence of the misalignment of the RPA and wire source axis. As a matter of fact, the angle  $\alpha$  between the line connecting the RPA collector to the accelerating electrode hole centre and the wire source axis increases ( $|\alpha| \leq 15^\circ$ ) as the measurement point moves away from the on-axis position. Consequently the projection of the  $z$  velocity component measured by the RPA decreases proportionally to the cosine of the angle  $\alpha$ .

In addition, using the WIPS in various gases permits discrimination of the parameters of influence on the beam spot size among the various variables (e.g.  $V_d$ ,  $V_f$ ,  $I_s$ ). As a rule, the beam spot size extension in both directions can be explained as follows.

Remembering that the electric field in the WIPS is well approximated in front of the extraction area by a sole radial component and considering ions created with zero initial kinetic energy, a typical ion trajectory in this region follows the radial electric field lines. Under this assumption, ion velocity  $v$  is simply aligned on the local radial unitary vector as shown in figure 11. Noting that the  $x$  and  $y$  axis are, respectively,

along the wire anode and the  $r_s \times z_s$  axis, the ion velocity  $v$  is just

$$v = v_0[\sin(\theta_s) \mathbf{y} + \cos(\theta_s) \mathbf{x} \times \mathbf{y}]. \quad (3)$$

Consequently, the ion beam projected in a plane perpendicular to the  $y$  axis features parallel ion trajectories (figure 11(a)). Conversely, the ion beam appears as a diverging beam in a plane perpendicular to the  $x$  axis (figure 11(b)); an increase in the WIPS discharge voltage results in a larger  $v_y$  without modifying the beam divergence.

The combination of the diaphragm and the accelerating electrode hole acts as an electrostatic lens. Due to the large value of the ratio  $d/R_e = 4$ , the focal length of this system is not strictly a decreasing function of  $V_s/V_d$  as opposed to an ideal two-cylinder electrostatic lens [14], but a function  $f_l$  of both parameters  $V_s$  and  $V_d$  such that  $\partial f_l / \partial V_d > 0$  and  $\partial f_l / \partial V_s < 0$ . Nevertheless, the two-cylinder formulae can be used as a first-order approximation of the focal length of the system. Looking at the  $x$  extension of the beam (figure 11(a)), increasing  $V_f = V_s - V_d$  for a given WIPS discharge voltage  $V_d$  decreases the focal length and hence yields a larger lens magnification. As illustrated in figure 12, the beam spot size indeed extends in the  $x$  direction when  $V_f$  is increased.

A refined explanation of the  $x$  extension of the beam is obtained by considering the Laplacian electric potential distribution in the system. Due to the electrodes configuration, isopotential lines corresponding to electric potentials lower than the WIPS cathode potential  $V_f$  penetrate into the diaphragm, as shown in figure 13. This isopotential line distribution creates a radial electric field localized in the diaphragm which is responsible of the mirror image observed in the  $x$  direction. Indeed, an inward radial momentum is transferred to the incoming parallel ion beam, yielding a converging ion beam. Moreover, as the accelerating electrode potential is increased, the isopotential lines penetrate further into the diaphragm, leading to a higher electric field and thus a shorter focal length.

**Table 2.** Radii of the cylinders surrounding, respectively, 50% and 80% of the total beam current for various  $\text{He}^+$  beam conditions.

Accelerating voltage $V_f$ (kV)	Plane id	50% radius (mm)	80% radius (mm)
2	$\mathcal{A}$	1.6	2.7
3	$\mathcal{A}$	2.3	3.7
4	$\mathcal{A}$	2.7	4.2
2	$\mathcal{B}$	2.4	3.9
3	$\mathcal{B}$	3.1	4.6

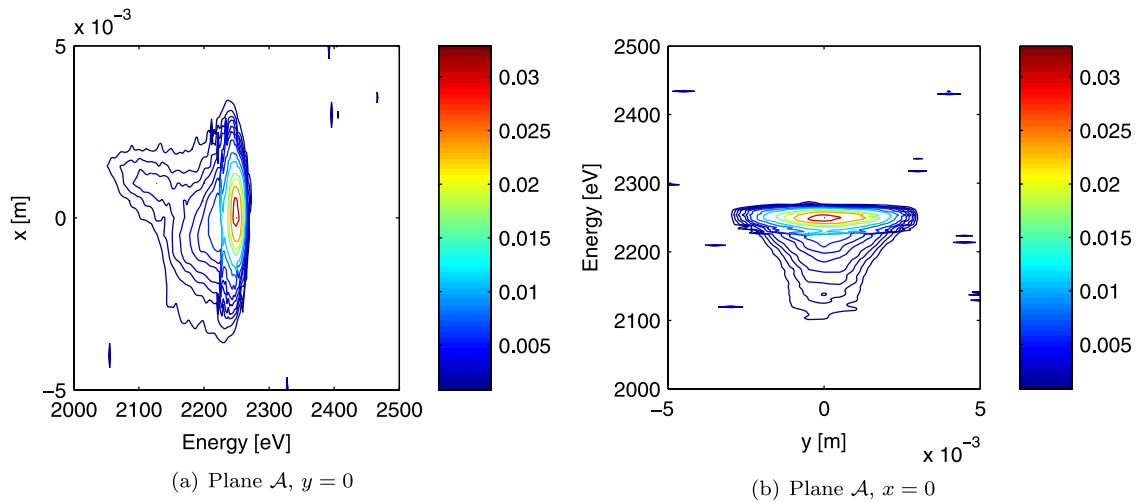


**Figure 10.** Isolevels of the dimensionless energy distribution function along the  $y$  (a) and  $x$  (b) axis for a  $10 \mu\text{A}$   $\text{He}^+$  beam. The accelerating voltage is 2 kV.



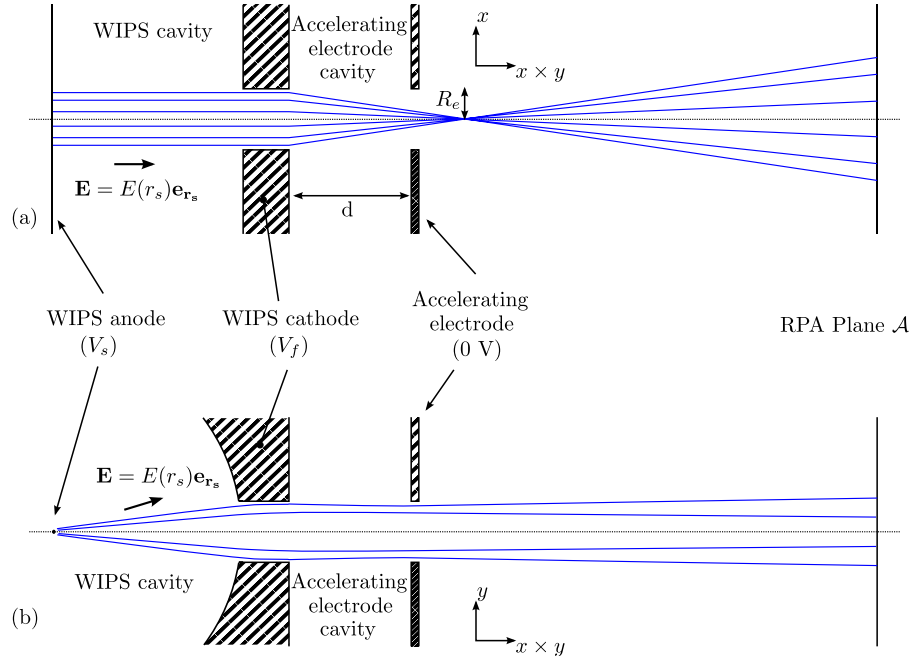


**Figure 11.** Image of the ion distribution formed by the electrostatic lens. The focal length is a decreasing function of the accelerating voltage  $V_f$  and an increasing function of WIPs discharge voltage  $V_d = V_s - V_f$ .

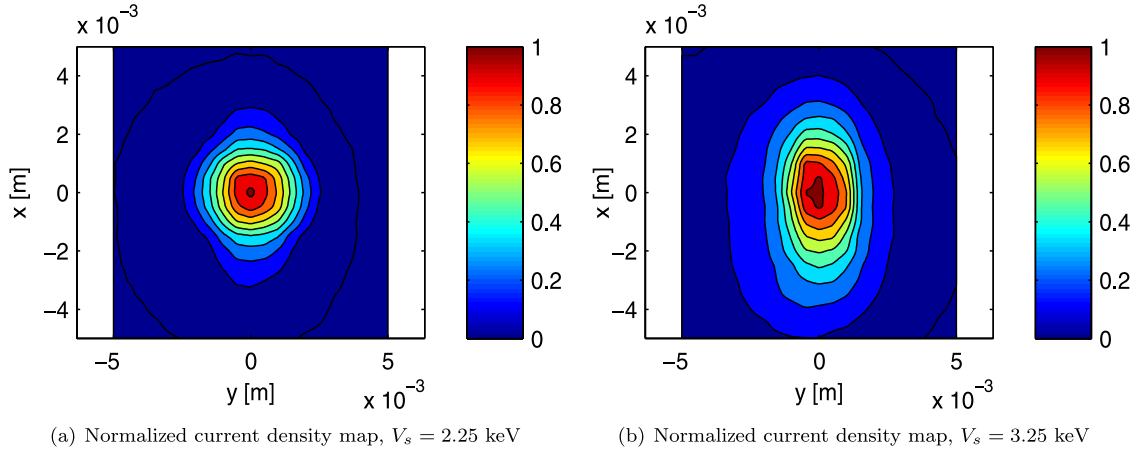


**Figure 12.** Normalized current density maps in plane  $\mathcal{A}$  for the same discharge condition in helium, but for two (a) and three (b) kilovolts of accelerating voltage. The beam spot size increases mainly in the  $x$  direction.

The role played by the radial electric field localized inside the diaphragm on the  $y$  beam extension can be synthesized as follows. As opposed to the  $x$  extension, ions penetrate into the diaphragm with a non-null velocity component in the  $y$  direction ( $v_y \neq 0$ ), in a way similar to light rays originating from a point source. Therefore, the ion beam extension in the  $y$  direction depends on the modification induced on  $v_y$  by the radial electric field while ions cross the diaphragm. For large  $V_s/V_f$  values, the potential well induced by the isopotential lines bending inside the diaphragm is shallow compared with the ion kinetic energy in the  $y$  direction, so that the sign of the  $v_y$  velocity component remains unchanged along the diaphragm crossing. Thus the image is a non-inverted diverging beam of which the divergence and the  $y$  extension are increasing functions of the ratio  $V_s/V_f$ . On the other hand, below a threshold value of  $V_s/V_f$ , the radial electric

field is sufficiently strong to straighten up the ion trajectory— $v_y = 0$ —at a certain distance inside the diaphragm. In this case, the situation of a parallel ion beam similar to the one described for the  $x$  extension of the beam is recovered. The image is consequently an inverted image, and hence the divergence and the  $y$  extension of the beam are decreasing functions of  $V_s/V_f$ .

The dependence of the  $y$  beam spot extension on  $V_s$  and  $V_f$  is well illustrated by three different cases. First, as shown in figure 14, comparable values of  $(V_s, V_f)$  corresponding to WIPs discharge voltages  $V_d = V_s - V_f$  of about 390 V and 415 V in argon and xenon and the same accelerating voltage  $V_f = 2$  kV lead to similar beam spot sizes despite of a large variation in terms of beam current. Second, the larger  $y$  extension observed in figure 14(a) compared with figure 12(a) for the same accelerating voltage  $V_f$  and a larger  $V_d$  (390 V

and 225 V) indicates that the beam extension in the  $y$  direction increases with  $V_s = V_d + V_f$ . Third, probing the ion beam obtained for the same WIPS discharge voltage  $V_d = 390$  V in argon and a higher  $V_f$  (lower  $V_s/V_f$ ) features a smaller extension in the  $y$  direction. These last two results corroborate the fact that the divergence of the beam is an increasing function of  $V_s/V_f$ , which is consistent with the explanation given for high  $V_s/V_f$  ratios.

The interpretation of the beam extension in both directions has been conducted neglecting the space charge phenomenon. The validity of this assumption can be verified *a posteriori* by evaluating the space charge electric potential inside the diaphragm. Ion number densities in the diaphragm corresponding to a  $20 \mu\text{A}$  ion current ( $1.25 \text{ A m}^{-2}$ ) extracted from the WIPS range between  $2.4 \times 10^{13} \text{ m}^{-3}$  in helium to and  $1.0 \times 10^{14} \text{ m}^{-3}$  in xenon, leading to electric potential differences of 1.7 to 7.2 V between the diaphragm axis and the diaphragm walls. In the meantime, potential differences ranging between 20 and 150 V are measured when computing the Laplacian electric potential distribution (figure 11). The

influence of the space charge induced electric field is therefore much limited and the Laplacian approximation is hence appropriate.

To summarize, ion beam currents of up to a few tens of microamperes have been obtained for various ionic species. Irrespective of ionic species, the spatial broadening of the beam spot size can be broken down into two contributions. The  $x$  extension is controlled by the ratio  $V_s/V_d$  and features an inverted image of the ion distribution in the WIPS on the range of potentials considered. Regarding the  $y$  extension, low values of  $V_s/V_f$  lead to the same behaviour as the one observed in the  $x$  direction whereas increasing  $V_s/V_f$  above the threshold value yields a non-inverted image.

## 5. Summary

Particle-in-cell (PIC) simulation of a low pressure ( $10^{-4}$ – $10^{-2}$  mbar) dc wire-induced plasma source reveals its high-pressure discharge mode to be a good candidate for the production of narrow-band ion beams.

In order to capitalize on this specificity, an experimental setup enabling the acceleration of an ion beam extracted from a low pressure dc wire discharge is reported. Retarding potential analyser (RPA) measurements corroborate the numerical results: operating the WIPS in its low-pressure mode leads to a broad-band energy distribution whereas a narrow-band ( $\sim 20$  eV) ion beam is produced when pressure is increased above the WIPS mode transition threshold pressure ( $\sim 10^{-2}$  mbar). Operating the WIPS in various gases shows that this behaviour is independent of the beam ionic species. Varying the accelerating electrode potential results in a simple shift of the energy distribution function, authorizing in turn a fine tuning (1–5 keV) of the beam energy. Analysis of the various contributions to the beam energy slight broadening compared with the PIC prediction suggests that the beam energy distribution width could be reduced to 10 eV using a voltage driven WIPS.

Three-dimensional RPA probing of the ion beam axial velocity component in the plume demonstrates that the ion

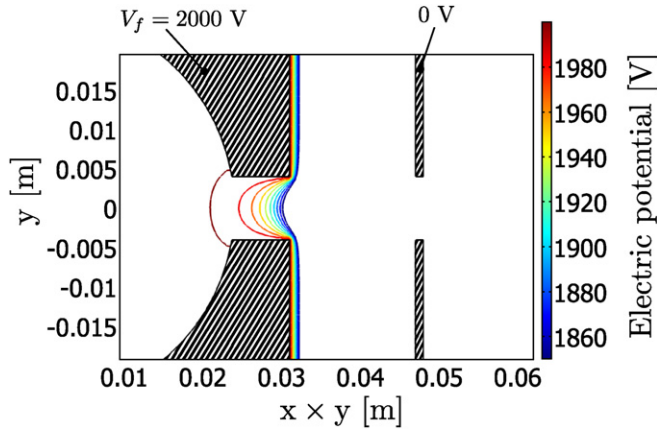


**Figure 13.** Isopotential lines for electric potential just below  $V_f$  ( $V_f = 2$  kV and  $V_d = 200$  V). The radial electric field resulting from the penetration of isopotential lines into the diaphragm is responsible of the beam extension in both directions  $x$  and  $y$ .

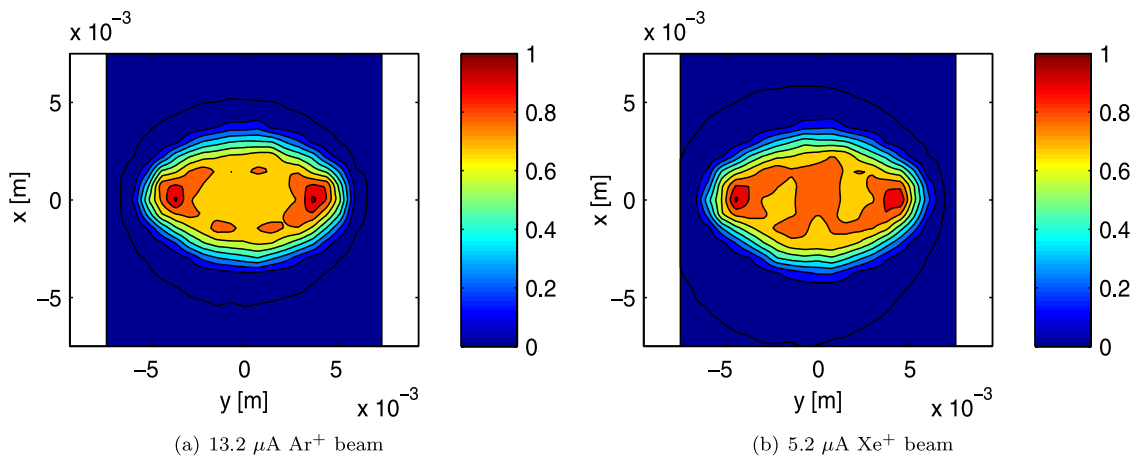


**Figure 14.** Normalized current density maps in plane  $\mathcal{A}$  of  $\text{Ar}^+$  (a) and  $\text{Xe}^+$  (b) beams at  $V_f = 2$  kV. The WIPS operating conditions are (a)  $I_s = 10$  mA and  $V_d \sim 390$  V, (b)  $I_s = 4$  mA and  $V_d \sim 415$  V. The increase in the beam spot size observed for both  $\text{Ar}^+$  and  $\text{Xe}^+$  compared with  $\text{He}^+$  results from a higher WIPS discharge voltage.

beam spot size is very limited, 80% of a  $10\ \mu\text{A}$   $\text{He}^+$  beam at 2.3 keV being contained in a 3 mm radius cylinder at 6 cm of the accelerating electrode. Comparison of data for two planes 5 cm apart indicates a divergence of about one degree. In addition, the local ion energy distribution function is shown to be almost uniform on the whole beam extension. Furthermore, the beam spot size extension can be broken down into two components. Extension of the beam along the WIPS wire anode is an inverted image of the ion distribution inside the WIPS whose size scales with the ratio  $V_s/V_d$ . On the other hand, the image in the perpendicular direction can be inverted or not depending on the value of the same ratio  $V_s/V_f$ .

Considering the fact that the focal length of the electrostatic lens formed by the diaphragm and the accelerating electrode hole determines the  $x$  extension of the beam spot size, a fine tuning of the distance between the diaphragm and the accelerating electrode should permit optimization of the current density for a given accelerating voltage. Moreover, enhancing the electron confinement in the WIPS would enable one to operate the WIPS at a lower discharge voltage  $V_d$ , decreasing in turn the beam spot size extension in the  $y$  direction as well as the power consumption.

## References

- [1] McClure G W 1963 *Appl. Phys. Lett.* **2** 233–4
- [2] Fitch R K, Mulvey T, Thatcher W J and McIlraith A H 1970 *J. Phys. D: Appl. Phys.* **3** 1399
- [3] Fitch R K and Rushton G J 1972 *J. Vac. Sci. Technol.* **9** 379–82
- [4] Rushton G J, O'Shea K R and Fitch R K 1973 *J. Phys. D: Appl. Phys.* **6** 1167–72
- [5] McIlraith A 1966 *Nature* **212** 1422
- [6] Clark W J and Dunning G 1978 *IEEE J. Quantum Electron.* **14** 126–9
- [7] Pigache D, Bonnet J and David D 1983 *Proc. 16th Int. Conf. on Phenomena in Ionized Gases (Dusseldorf)*
- [8] Urai H, Kurosawa T, Okino A, Hotta E, Yasui H, Tamagawa T and Ko K C 1997 *Rev. Sci. Instrum.* **68** 3346–50
- [9] Pigache D 1987 *Proc. 18th Int. Conf. on Phenomena in Ionized Gases (Swansea, UK)* vol 4 pp 782–3
- [10] Gueroult R, Elias P Q, Packan D, Bonnet J and Rax J M 2010 *J. Phys. D: Appl. Phys.* **43** 365204
- [11] Kaminsky M 1965 *Atomic and Ionic Impact Phenomena on Metal Surfaces* (Berlin: Springer)
- [12] Szapiro B, Rocca J J and Prabhuram T 1988 *Appl. Phys. Lett.* **53** 358–60
- [13] Enloe C L 1994 *Rev. Sci. Instrum.* **65** 507–8
- [14] Harting E and Read F 1976 *Electrostatic Lenses* (Amsterdam: Elsevier)